THE UNIVERSITY of EDINBURGH

Edinburgh Research Explorer

Simple lattice model explains equilibrium separation phenomena in glassy polymers

OPEN ACCESS

Simple lattice model explains equilibrium separation phenomena in glassy polymers

Tianmu Yuan,[1, *] Maria Grazia De Angelis,[2] and Lev Sarkisov[1]

[1]*Department of Chemical Engineering, the University of Manchester*
[2]*Institute for Materials and Processes, School of Engineering, the University of Edinburgh*

The Robeson bound is a theoretical limit that applies to kinetics-driven membrane separations of gas mixtures. However, this bound does not apply to sorption-driven membrane processes such as CO_2/N_2 separation, which lacks a theoretical explanation. As a result, we are uncertain about the factors that control the limiting behavior of sorption-driven separations. To address this issue, we employed a simple lattice model and dynamic mean field theory to examine the transport properties of disordered model structures, isolating sorption effects from purely kinetic effects. Our findings indicate that transport effects play a crucial role in sorption-driven processes, and perm-selectivity is consistently lower than sorption selectivity, which is an unattainable limit. We used basic geometric fragments of the structure to explain how transport effects emerge and manifest themselves in sorption-driven processes.

I. INTRODUCTION

Membrane technologies for gas separations are considered to be an energy efficient alternative to the traditional absorption processes. [1, 2] Membranes can be broadly classified into two categories based on the material: organic (polymer) membranes and inorganic/metallic membranes. Recently, new classes of membranes have emerged based on graphene materials[3, 4] and Metal-Organic Frameworks[5]. Polymeric membranes are still the most widely used type of membrane for industrial gas separation compared to inorganic membranes such as zeolite, ceramic, metallic, and carbon-based membranes, due to their favorable combination of cost-effectiveness, good mechanical and chemical stabilities, and excellent separation performance.[6, 7] The separation performance of a membrane process is governed by two key characteristics of the polymer material: permeability and perm-selectivity. These characteristics are, however, in competition with each other: polymers with high permeability do not exhibit high selectivity and vice versa. Robeson clearly demonstrated this trade-off by compiling a large amount of data for the performance of various polymer materials and different gas couples and by plotting perm-selectivity as a function of permeability on log–log scale [8, 9]. Moreover, generalizing these trends, Robeson noted that the trade-off between perm-selectivity and permeability must lead to a practical limitation (now known as the Robeson bound) to the performance of polymer materials in separation of a particular gas pair. [8, 9] This empirical observation played an important role in assessing the economic potential of the membrane separation processes and in guiding various strategies to modify polymer materials. For example, a strategy where properties of two materials (polymer and filler) are combined in order to overcome the Robeson limit led to the development of the mixed matrix membranes [10, 11].
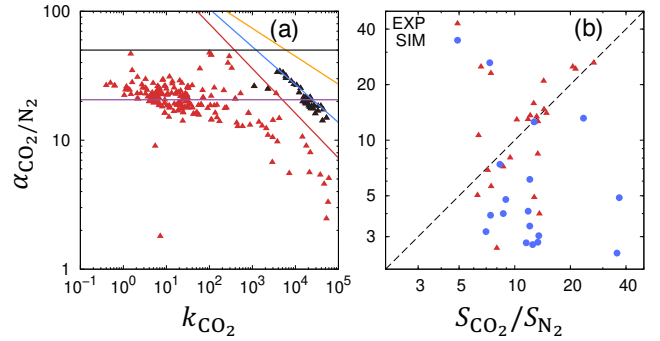
* tianmu.yuan@manchester.ac.uk

FIG. 1. CO_2/N_2 perm-selectivity as a function of (a) CO_2 permeability [12–31] and (b) sorption selectivity for various glassy polymer membranes[22–31]. In panel (a), the red, blue, and yellow lines are the upper bounds from Robeson [9], Comesaña-Gándara et al. [21], and Freeman [32], respectively. The black line is a hypothetical upper bound based on the highest selectivity available where the purple line is the selectivity calculated from Eq. 4. The black triangles in panel (a) highlight membranes based on PIMs. In panel (b), results from experiments and simulations are shown as red triangles and blue circles, respectively.

Several theoretical justifications for the Robeson bound have been proposed. [20, 32–35] In the notable contribution by Freeman [32], the starting point is the solution-diffusion theory, which considers permeability as a product of of solubility S and diffusivity D:

$$k = SD \tag{1}$$

The perm-selectivity for species A and B, $\alpha_{A/B} = \frac{k_A}{k_B}$, can be then divided into two contributing factors: sorption selectivity $(\frac{S_A}{S_B})$ and diffusion selectivity $(\frac{D_A}{D_B})$. Depending on which contribution dominates the process, we can distinguish sorption-driven or kinetics-driven separation. [36] Colloquially speaking, sorption-driven separation exploits different levels of affinity of the components of the mixture towards the polymer material.

Higher concentration of the stronger binding component in the membrane should lead to a higher flux of this component across the membrane, and, hence, the permeate stream should be enriched in this component. Conversely, kinetics-driven separation can be thought of as a sieving mechanism that discriminates between species based on their molecular size and the resulting free energy barriers to cross narrow windows in the polymer structure. In the kinetics-driven separations, the permeate product should be enriched in the component with a smaller molecular size. This component is also expected to have weaker interactions with the polymer material compared to the component with larger molecular size.

Freeman's theory views separation in membranes as a predominantly kinetics-driven process, with the diffusion selectivity expressed as a function of the kinetic diameter (d) of the gas molecules:

$$\ln\left(\frac{D_A}{D_B}\right) = \left(\frac{1-a}{RT}\right)c(d_B^2 - d_A^2) \qquad (2)$$

where a and c are constants, R and T are gas constant and temperature, respectively. This approach is expected to work well for gas pairs such as H_2/CH_4 or He/N_2, with a significant difference in molecular size between the two species. [32]

However, a very important case of CO_2 and N_2 separation for carbon capture applications cannot be described by this theory. A compilation of data for CO_2/N_2 separation for glassy polymers on a Robeson plot is shown in Fig. 1a. On the same figure, we also show two empirical upper bounds (red and blue lines) drawn based on the experimental results [9, 21], as well as a theoretical prediction based on Freeman's work (yellow line) [32]. From this, we can say that it is difficult to discern a well defined boundary similar to other pairs of gases. In fact, as shown in Fig. 1a, several possible boundaries could be drawn, possibly controlled by very different mechanisms.

Let us briefly summarize what is known about CO_2/N_2 separation and how it is different from the kinetics-driven processes. Firstly, CO_2 and N_2 have relatively similar kinetic diameters ($d_{CO_2} = 0.33$ nm and $d_{N_2} = 0.364$ nm, respectively) and the arguments in the foundation of the kinetics-based theories play a diminished role here. However, transport effects do play an important role in CO_2/N_2 separation. This is easy to show by naively assuming that $\frac{D_{CO_2}}{D_{N_2}} \approx 1$, leading to

$$\alpha_{CO_2/N_2} = \frac{k_{CO_2}}{k_{N2}} \approx \frac{S_{CO_2}}{S_{N_2}} \qquad (3)$$

The result above is also an outcome of the Freeman's theory if one assumes $d_{CO_2} = d_{N_2}$. If the Eq. 3 were true, it would give us a useful insight on the limiting behavior of the polymer materials. For example, in the limiting case of infinite dilution, the solubility (S_0) is dominated by the gas condensability, usually associated with its critical temperature (T_C), and the sorption selectivity can then be expressed as: [37, 38]

$$\frac{S_{0,CO_2}}{S_{0,N_2}} \approx \exp\left[b_0(T_{c,CO_2} - T_{c,N_2})\right] \qquad (4)$$

where b_0 is a constant usually taken as 0.017 K^{-1}. This brings the selectivity to an approximate value of 20.6 for CO_2/N_2 separation [37, 38] and this boundary is also indicated in Fig. 1a by the purple line.

However, the Eq. 3 is generally not valid. Fig. 1b compiles data for polymers for which data for α_{CO_2/N_2} and $\frac{S_{CO_2}}{S_{N_2}}$ is available. While Eq. 3 applies to several polymers, there are groups of materials with both $\alpha_{CO_2/N_2} > \frac{S_{CO_2}}{S_{N_2}}$ and $\alpha_{CO_2/N_2} < \frac{S_{CO_2}}{S_{N_2}}$ deviations from the parity plot, clearly indicating the importance of transport effects.

Secondly, unlike H_2/CH_4 or He/N_2 separations where the product is the weakly adsorbing component, in CO_2/N_2 separation, we are interested in the strongly adsorbing component, CO_2. The concentration of CO_2 will be higher in the membrane than that of N_2, contributing to the flux, and this has been considered as the primary driver for separation.

Another possible angle of analysis stems from some similarities between high porosity glassy polymers such as polymers of intrinsic microporosity (PIMs) and crystalline porous materials such as zeolites and Metal Organic Frameworks (MOFs). PIMs have been considered as promising membrane materials for CO_2/N_2 separation. [21] Here, the structure consists of rigid units forming connected porous spaces. They can be seen as an amorphous counterpart to crystalline MOFs. From the theoretical considerations, nanoporous materials, such as zeolites and MOFs, should behave very differently from the dense polymers, and in fact for zeolites it has been shown that the overall selectivity increases with permeability - which is the opposite trend to the Robeson boundary as shown in Fig. 1a. [39]

Based on these considerations, it appears that a comprehensive theoretical framework for adequately explaining sorption-driven separation in glassy polymers, analogous in terms of the level of theoretical rigour and insight to the Freeman's theory for kinetics-driven separation, is currently lacking. Without a clear understanding of the factors that determine the theoretical limits of sorption-driven separation, it is not feasible to rationally design new polymer materials.

In principle, this understanding could be formed using molecular simulations. [40] In particular, adsorption behavior in models of polymers with permanent porosity can be obtained using Grand Canonical Monte Carlo (GCMC) approaches. Self-diffusion coefficients are routinely obtained using molecular dynamics. [41] Non-equilibrium simulations of transport across a model membrane driven by the gradient of chemical potential can be

used to directly obtain permeability of species either as single components or mixtures. Therefore, theoretically, it is possible to calculate independently all the terms in Eq. 1 and explore transport properties of the membrane as a function of various parameters. However, this is not the common practice due to the enormous computational cost associated with the direct simulation of permeation across a model membrane in fully atomistic molecular simulations. [42, 43] As a result, a typical molecular simulation study obtains sorption properties (e.g. solubility coefficient) and self-diffusion coefficient, and uses them to derive all other properties of the membrane (permeability, perm-selectivity). In experiments, typically k and S are obtained from independent measurements, and D is derived using the solution-diffusion relation. [44] Another common practice is to measure k and D from the time-lag method and calculate S using the solution–diffusion model. [45, 46] Not surprisingly, this leads to different predictions from the molecular simulations and experiments. In particular, as shown in Fig. 1b, molecular simulations consistently predict lower self-diffusion coefficient values for CO_2 compared to N_2. Transport diffusion coefficients from the experiments, on the other hand, derived from S and k, show similar values for CO_2 and N_2, and sometimes even higher transport diffusion rates for CO_2 [22–31]. This results in molecular simulations typically predicting $\alpha_{CO_2/N_2} < \frac{S_{CO_2}}{S_{N_2}}$, whereas in experiments the picture is more complex, as seen from Fig. 1b.

The factors discussed above have inspired the present study. Our goal is to create a simple theoretical method and a model to calculate the permeability of model membranes with complex geometries. We aim to establish a connection between the permeability and perm-selectivity of the model with the topology of its structure and the interactions between the guest species and the host matrix.

For this, we employ a lattice model of the system coupled with the dynamic mean field theory (DMFT). [47, 48] The detailed description of the theory and the model is provided in the Methods section. Briefly, in the lattice model, the system of interest consists of discrete lattice sites. Each site can be occupied either by a fluid particle, a solid particle representing adsorbent or membrane material, or be empty. Only nearest-neighbour site interactions are considered. The mean field theory replaces the actual occupancy of the sites with the average density and provides an analytical solution to the fluid density at a given chemical potential or bulk pressure. Transport on the lattice sites can be viewed as hopping of particles from one site to another. In the dynamic version of the mean field theory, transport of the particles is replaced with density current between the sites which again can be solved analytically in the presence of external gradients of pressure, concentration, or chemical potential. The DMFT is a qualitative theoretical framework which has been applied extensively in the field of adsorption, capillary condensation, and dif-

fusion in porous materials. [47–68] Previously, we have demonstrated the applicability of the DMFT to study single-component fluid transport under non-equilibrium conditions by comparing the results from the DMFT to the molecular dynamic simulations using simple slit pore geometries[69]. In a consequent study, we applied this theory to describe transport in more complex heterogeneous media. [70] It is important to note that the language of the lattice model is very general and not limited to representing polymer materials. The main reason for focusing on polymer membranes in this study is the abundance of experimental data available for these materials, including generalizations represented by the Robeson plot, and their wide use in industry.

Herein, we extend our previous work by using the two-component DMFT to study fluid separation phenomena in lattice models of polymers. Theoretical and simulation studies in general allow us to decouple complex physical phenomena by creating appropriate hypothetical systems. In particular, in this work, the underlying parameter that describes the frequency of particle hops from one lattice site to another takes the same value for both species of the binary mixture. This makes it possible to investigate sorption, transport, and separation behavior emerging solely from the interaction of the particles with the polymer structure and from the topology of this structure. Using this approach, the solubility, permeability, and selectivity trends as a function of polymer matrix density and solid–fluid interactions are investigated for single-component systems and binary mixtures. We visualize the flux and local perm-selectivity for polymers to explain the separation mechanism within complex geometries. Finally, we link our observations to the experimental results to enhance our understanding of sorption-driven separation mechanisms in membranes.

II. METHODS

A. Mean field theory

The theoretical framework applied in the work closely follows the work by Edison and Monson [47, 48], and we refer the readers to the original article for additional details.

1. Static mean field theory

We start by considering a simple cubic lattice system with nearest neighbour interactions under an external field ψ. An example of a 4×4 system is illustrated by Fig. 2, where its sites are labelled between 1–16. Each site can be occupied by either a fluid particle (gray), a solid particle (red), or being empty. Pair-wise interactions between site 3 and 7, 7 and 11 are included as we only consider nearest neighbour interactions. Therefore,
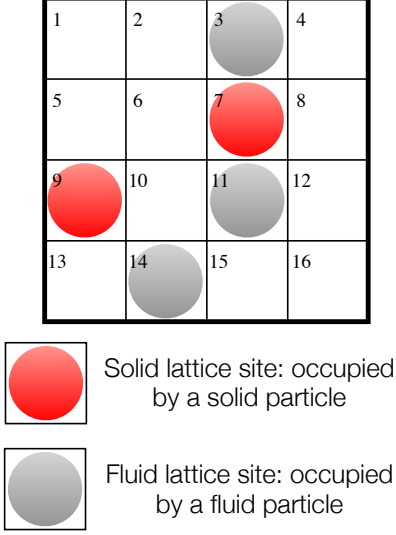
FIG. 2. An example of a 4×4 cubic lattice system, red and gray spheres are solid and fluid particles, respectively.

the Hamiltonian for a two-component system with fluid species A and B in an external field ψ can be written as

$$H = -\frac{1}{2}\sum_i \sum_j \sum_a \sum_b \epsilon_{ab} n_i^a n_j^b + \sum_i \sum_j n_i^a \psi_i^a \quad (5)$$

where a and b denote the fluid species and can be either A and B, ϵ_{ab} describes the interaction between fluid a and b. The fluid occupancy for site i is denoted as n_i which can be either 0 (unoccupied) and 1 (occupied), j represents the nearest neighbour of site i ($j \neq i$). The external field at site i, ψ_i, can be expressed as

$$\psi_i^a = -\epsilon_{sa} \sum_j (1 - \eta_j^a) \quad (6)$$

where ϵ_{sa} describes the solid–fluid interaction between solid s and fluid a, and η_j is the solid occupancy at site j. The value for η can be either 0 (occupied) or 1 (unoccupied).

The mean field treatment leads to the following expression for the Hamiltonian

$$H_{MF} = \frac{1}{2}\sum_i \sum_j \sum_a \sum_b \epsilon_{ab}\rho_i^a \rho_j^b - \sum_i \sum_a n_i^a \left(\sum_j \sum_b \epsilon_{ab}\rho_j^b - \psi_i^a\right) \quad (7)$$

where $\rho = \langle n \rangle$ is the dimensionless average occupancy or the density. The grand potential of the system can then be written as

$$\Omega = -\frac{1}{2}\sum_i \sum_j \sum_a \sum_b \epsilon_{ab}\rho_i^a \rho_j^b + \sum_i \sum_a \rho_i^a(\psi_i^a - \mu_i^a) + k_{\mathrm{B}}T \sum_i \left[\sum_a (\rho_i^a \ln \rho_i^a) + (1 - \sum_a \rho_i^a)\ln(1 - \sum_a \rho_i^a)\right] \quad (8)$$

where μ is the chemical potential and k_{B} is the Boltzmann constant. The minimization of the grand potential with respect to density gives the density distribution at equilibrium,

$$k_{\mathrm{B}}T\left[\ln \rho_i^a - \ln\left(1 - \sum_b \rho_i^b\right)\right] - \sum_j \sum_b \epsilon_{ab}\rho_j^b + \psi_i^a - \mu_i^a = 0 \quad \forall a, i \quad (9)$$

The above equation can be solved iteratively for a density distribution at fixed chemical potentials for the individual species at a given temperature.

2. Dynamic mean field theory

The dynamic behavior of the system closely follows the work by Gouyet et al. [71] and Monson et al. [48]. The readers are referred to the original articles for additional details.

We start by expressing the change in density at site i with respect to time,

$$\frac{\delta \rho_i^a}{\delta t} = -\sum_j J_{i,j}^a \quad (10)$$

where $J_{i,j}^a$ is the flux of species a from site i to its nearest neighbour j. Considering the Kawasaki dynamics which generates dynamics via nearest neighbour hopping processes, the flux from site i to its nearest neighbour j can be formulated as

$$J_{i,j}^a = \omega_{i,j}^a \rho_i^a (1 - \sum_b \rho_j^b) - \omega_{j,i}^a \rho_j^a (1 - \sum_b \rho_i^b) \quad (11)$$

where $\omega_{i,j}^a$ is the transition probability of hopping for species a from site i to j based on the Metropolis criteria. This can be expressed as

$$\omega_{i,j}^a = \omega_0^a \exp\left(\frac{-E_{i,j}^a}{k_{\mathrm{B}}T}\right) \quad (12)$$

where

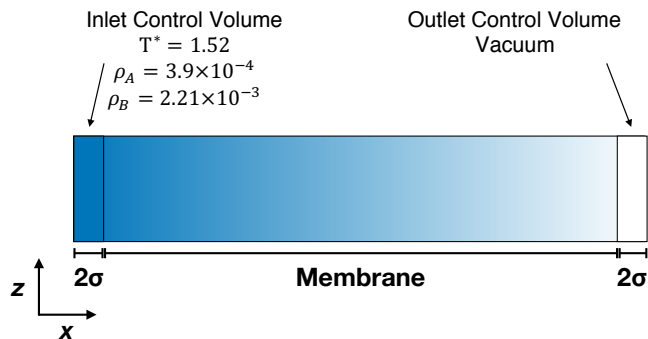$$E_{i,j}^a = \begin{cases} 0, & E_j^a < E_i^a \\ E_j^a - E_i^a, & E_j^a \geq E_i^a \end{cases} \quad (13)$$

FIG. 3. A schematic diagram of the non-equilibrium set up. The inlet and outlet control volumes are place on the left and right side of the membrane, respectively. The term σ is the unit length of the lattice and the control volumes are made of two layers of lattice sites.

and

$$E_i^a = -\sum_j \sum_b \epsilon_{ab} \rho_j^b + \psi_i^a \qquad (14)$$

In the case of a steady state condition $\frac{\delta \rho_i^a}{\delta t} = 0$, the flux can be rewritten as

$$J_{i,j}^a = \omega_{i,j}^a \rho_i^a (1 - \sum_b \rho_j^b) \left[1 - \exp\left(\frac{\mu_j^a - \mu_i^a}{k_B T} \right) \right] \qquad (15)$$

Both Eq. 11 and 15 can be used to solve the dynamics transport behavior of the system. Throughout this work, unless otherwise specified, Eq. 11 will be used.

B. Model details

To study the membrane separation processes based on pressure/chemical potential gradient, we setup an non-equilibrium condition by placing two control volumes on either side of the membrane. A schematic diagram is shown in Fig. 3. Although the theoretical framework employed here is qualitative in nature, we aimed to correlate the conditions of actual carbon capture from power plant flue gas with the phase diagram of the lattice gas. Specifically, we set the inlet condition of the membrane to match the output from a coal power plant. For simplicity, we assume an inlet stream consisting of 15% carbon dioxide (referred to as component A) and 85% nitrogen (B), at a pressure of 1 bar and a temperature of 308.15 K. In the lattice model, this corresponds to an inlet with $\rho_A^* = 3.9 \times 10^{-4}$ and $\rho_B^* = 2.21 \times 10^{-3}$. The chemical potential for each components are $\mu_A^* = -11.94$ and $\mu_B^* = -9.30$. The outlet condition is set to vacuum $\rho_A^* = \rho_B^* = 0$. Furthermore, taking into account the mean field prediction for the critical temperature of a simple cubic lattice, $T_{crit}^* = 1.5$, we scale the system's temperature relative to the critical temperature to match the temperature ratio of the flue gas to the critical temperature of carbon dioxide, $T^* = \frac{308.15}{T_{crit,CO_2}^*} * T_{crit}^* \approx 1.52$ and the timescale ω_0 is set to 0.2 throughout the study.

In the preliminary studies on the sensitivity of the model to the initial conditions, we noted that permeability and perm-selectivity depend on the pressure of the gas mixture, its temperature, and composition. In this article, the conditions considered correspond to a specific scenario of carbon capture from flue gas. Focusing on this one specific condition allows us to explore the influence of the matrix density, decoupling it from all other factors and isolating the role of pore morphology in the transport phenomena.

The interaction strength is scaled with respect to the carbon dioxide self interaction strength, hence, $\epsilon_{AA} = 1$. The self interaction for nitrogen is scaled according to the critical temperature $\frac{\epsilon_{BB}}{\epsilon_{AA}} = \frac{T_{c,N_2}}{T_{c,CO_2}}$, therefore, $\epsilon_{BB} = 0.415$. The interaction between fluid A and B, $\epsilon_{AB} = \sqrt{\epsilon_{AA}\epsilon_{BB}} = 0.644$. The interactions between fluid and solid are listed in Table I. All the polymer systems have system sizes of 200×50 lattice spaces. If we take the diameter of CO_2 as the base unit, this corresponds to ≈66nm thick which falls in the range of thin-film membranes.

III. RESULTS AND DISCUSSION

In this work, the structure of glassy polymers is represented as a random distribution of lattice sites. We refer to each particular realization of this structure as a matrix. While conceptually simple, this approach captures several essential features of a glassy polymer, such as the rigidity of the structure and its amorphous, disordered nature. The key property of this structure is the volume fraction of solid lattice sites, ϕ_s. The fraction ϕ_s is varied between 0 (empty) and 0.40. At the highest value of ϕ_s, the volume fraction of the remaining empty space (0.60) corresponds approximately to the percolation threshold for square lattice systems. All the properties of interest are averaged over three independent realizations of the polymer matrix with a particular value of ϕ_s.

Although the lattice model is cubic in nature, the third dimension is extended using the periodic boundary conditions, making the systems essentially 2D square lattices when considering the percolation threshold. We would like to note that this simple 2D lattice model does not capture the atomistic details of the polymer and cannot reproduce precise values of polymer properties such as

TABLE I. Solid–fluid interaction strengths for different polymers.

	C_1	C_2	C_3
ϵ_{sA}	5.3	1.7	5.3
ϵ_{sB}	3.413	1.095	0.623

porosity and fractional free volume (FFV). Instead, we view this model as a qualitative tool for exploring the relationships between porosity, solid–fluid interaction, and permeation patterns. This approach allows us to investigate the influence of these variables on transport phenomena and decouple this influence from other factors.

We consider the adsorption and diffusion of two gas species, A and B. While the presented theoretical model is qualitative and all the results are presented in arbitrary dimensionless units, several parameters associated with these two species are guided by the underlying problem of CO_2 and N_2 separation. Species A represents CO_2 and all interactions in the system are considered in units of fluid–fluid interactions for species A. The ratio of fluid–fluid interactions for species A and B is equal to the ratio of CO_2 and N_2 critical points. The model then effectively has only two free parameters: the strength of solid–fluid interactions and the volume fraction of the solid lattice sites, ϕ_s. To represent membranes with different polymer–fluid interactions, three combinations of solid–fluid interaction strengths are considered. In particular, in C_1 case both fluids interact strongly with the polymer; in C_2 case both fluids interact weakly with the polymer; and in C_3 case fluid A interacts strongly with the polymer, while B is weakly interacting. The actual values of the parameter ϵ_{sf} describing solid–fluid interactions for species f are a result of some preliminary experimentation with the model and are somewhat arbitrary. However, what is more important is the range of adsorption and transport scenarios emerging as a result of different interaction models.

Starting with C_1, ϵ_{sA} is set to 5.3 in dimensionless units, whereas ϵ_{sB} is scaled to maintain the ratio $\frac{\epsilon_{sA}}{\epsilon_{sB}} = \frac{\epsilon_{AA}}{\epsilon_{BB}}$. In C_2, ϵ_{sA} and ϵ_{sB} are scaled down by factor of 3 based on C_1. In case of C_3, ϵ_{sA} is the same as in C_1, but ϵ_{sB} is 5.5 times lower compared to the same parameter in C_1 to create a case with a particularly strong sorption selectivity of the system towards A, representing CO_2 (Table I).

We employ the static version of the mean-field theory to obtain adsorption behavior and solubility coefficients in model polymer matrices. To obtain permeability across the membrane, we employ the dynamic mean-field theory, as described in the Methods section.

We start with the equilibrium sorption calculations from static mean field theory (SMFT). The solubility (S) is obtained using the following equation,

$$S = \frac{\frac{1}{N}\sum_{i=1}^{N} \rho_i}{p} \tag{16}$$

where N, p, and ρ_i are the total number of sites, pressure, and density on site i, respectively. The calculated sorption selectivity is shown in Fig. 4a–4c. In this figure, the ideal results are obtained from pure component calculations and are compared with the results obtained for adsorption from binary mixtures under the same conditions as in the source control volume in the DMFT studies.
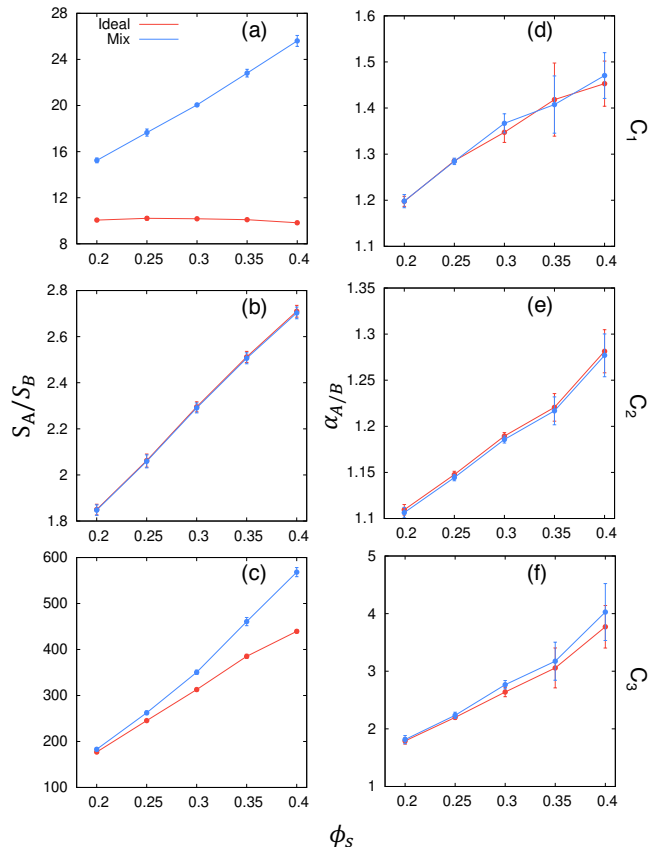

FIG. 4. Sorp- (a–c) and perm- (d–f) selectivity as a function of the fraction of solid lattice sites in the matrix ϕ_s for C_1–C_3 interaction cases, respectively. Red and blue lines show the results obtained from single component isotherms and from binary mixtures, respectively. The error bars are the standard deviations.

This data is complemented by the adsorption isotherms for single components and binary mixtures, presented in the Supplementary Material file. The isotherms, as depicted in the graphs, show linearity for weakly adsorbing species and in low density matrices, corresponding to the Henry's law regime. With increasing solid-fluid interactions and/or matrix density, the isotherms transition towards a shape resembling the Langmuir isotherm. Both properties, solubility at the inlet conditions, and equilibrium adsorption isotherms reveal the same trends. Large deviations between the ideal and mixture calculations are observed for C1. In this case, both fluids strongly interact with the solid structure and the competition for the binding sites cannot be captured by considering separately individual adsorption isotherms for pure components. In Fig. 4a, large deviations between the ideal and mixture calculations are observed for C_1. In this case, both fluids strongly interact with the solid structure and the competition for the binding sites cannot be captured by considering separately individual adsorption

isotherms for pure components. The differences are lessened when adsorption of one of the components strongly dominates over the other (C_3) and the results are almost identical if both components adsorb weakly (C_2) due to the reduced adsorption density and lack of competition for the available porous space. Notably, as expected, the selectivity grows with volume fraction of solid lattice sites ϕ_s due to the increased solid–fluid interactions.

The DMFT calculations were performed to establish a non-equilibrium steady state flux across the lattice structure. The outcome of the DMFT calculation is the local density and flux on each site, from which other properties can be derived. Eq. 17 is used to calculate the permeability

$$k = J \frac{L}{A' \Delta p} \tag{17}$$

where J, L, and A' are the total flux in the direction of pressure gradient, length of the membrane, and cross-sectional area of the membrane, respectively.

Fig. 4d–4f shows the perm-selectivity calculated using the DMFT. Firstly, for all the cases, the ideal perm-selectivity is in good agreement with the actual perm-selectivity calculated from mixtures. For C2, the perm-selecitivties from ideal and mixtures are almost identical, and there are small deviations for C1 and C3. This is stemmed from the competing effect between fluids which is not captured from single-component calculations. Nevertheless, this demonstrates the reasonable validity of using single component permeation data to predict the perm-selectivity for mixtures in agreement with many experimental observations, although systems where this assumption does not hold have also been reported. [72]

However, the most important observation from Fig. 4 is associated with the differences in the values of perm-selectivity and sorption selectivity. While the trend is the same for both properties, as selectivity increases with the density of the polymer, the values of perm-selectivity are much lower (as many as two orders of magnitude) compared to sorption selectivity, suggesting that the diffusion is playing a significant role in the fluid separation performance. This is also consistent with the experimental observations, where a large value of S can lead to the so-called "immobilising sorption" effect, where D, and hence the permeability k, are reduced. [73]

Using the lattice model, we can elucidate which transport effects contribute to the effective perm-selectivity in disordered structures.

For this, we visualize a particular system, C_3 polymer with $\phi_s = 0.43$ in Fig. 5. We note here that this structure has a somewhat higher fraction of solid lattice sites, and we employ this structure to emphasize and illustrate the topological effects. While in general, the fraction remaining available vacant lattice sites is below the percolation threshold for square lattice, we checked that the particular matrix realizations employed remain percolated with respect to fluid transport. The top panel in Fig. 5 shows
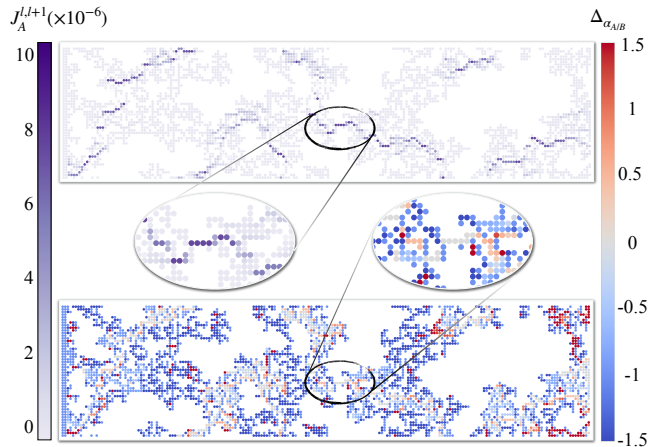

FIG. 5. Visualization of the flux distribution (Top) and visualization of the local selectivity difference (Bottom) in the polymer matrix with $\phi_s = 0.43$.

the local flux ($J_A^{l,l+1}$) distribution in the direction of fluid flow, and the bottom panel demonstrates the local selectivity difference ($\Delta_{\alpha_{A/B}}$) where the local selectivity ($\alpha_{A/B}^{\text{local}}$) is calculated from the following equation:

$$\alpha_{A/B}^{\text{local}} = \frac{J_A^{l,l+1}/\Delta p_A}{J_B^{l,l+1}/\Delta p_B} \tag{18}$$

where Δp is the pressure drop across the membrane. The local selectivity difference is defined as:

$$\Delta_{\alpha_{A/B}} = \frac{\alpha_{A/B}^{\text{local}} - \alpha_{A/B}}{\alpha_{A/B}} \tag{19}$$

The first thing to notice about this picture is the large areas coloured white, not showing any distribution of flux or local selectivity. These regions are spatially isolated from the rest of the structure and therefore nothing can diffuse in or out of these regions. Secondly, it is clear from the picture that the distribution of the flux and selectivity is very heterogeneous reflecting the disorder of the underlying matrix.

The specific system and matrix realization shown in Fig. 5 is employed here as a particularly strong illustration of the important role of the connectivity issues in the overall performance of the membrane. Indeed, the permeability across the whole structure shown in the figure hinges on a single passage or channel in the middle of the structure (shown in the ellipses in the figure). All molecules diffusing in the pressure gradient across this structure must pass through this channel. The local selectivity calculated for this crucial link is very close to the average overall perm-selectivity of the whole structure and it is much lower than the sorption selectivity for the same structure.
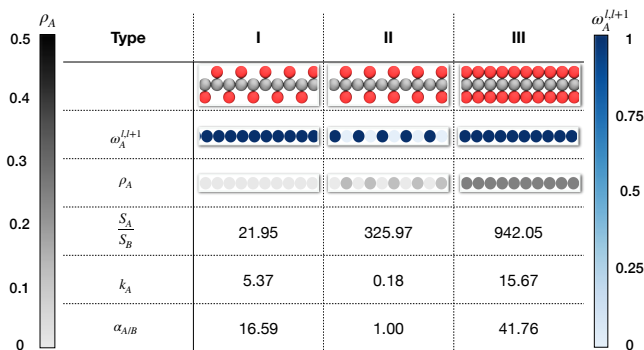
FIG. 6. Transport properties in a single channel with different arrangements of solid lattice sites forming the walls. The fluid and solid lattice sites are represented as grey and red spheres, respectively. The properties are calculated based on C_3 with a length of the system of 200 lattice sites. The black and blue colour bars represent the fluid density and the average hopping rate under steady state conditions of component A, respectively.
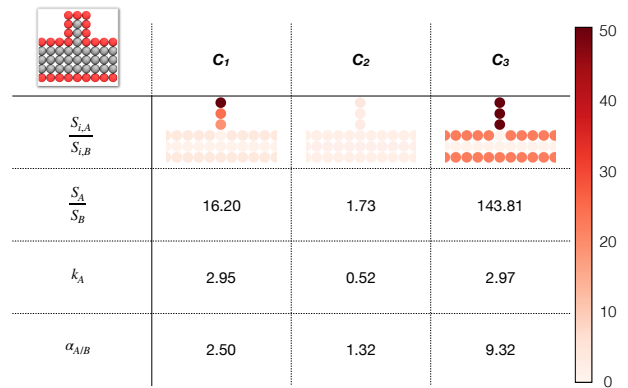

FIG. 7. Transport properties for a lattice fragment of a channel with a dead-end side-branch pore. The red and grey spheres represent solid and fluid lattice sites, respectively. This dead-end pore is repeated every 10 lattice sites and the system is in total 200 lattice sites long. The color bar shows the scale for the local sorption selectivity.

While this example is obviously an extreme case of connectivity-limited transport (due to a high volume fraction of solid lattice sites representing polymer), it is symptomatic for all model systems considered in this study.

It seems that in disordered structures such as the ones considered here, not all the regions contribute to the transport across the membrane and the regions that do contribute to the transport, may exhibit effective selectivity very different from what one would expect from the equilibrium sorption measurements.

We would like to illustrate the last statement by considering two very simplified toy models, which allow us to consider two specific effects in isolation.

The first simplified model system examines the influence of the energy barriers on the effective perm-selectivity. For this, we consider a structural element that consists of a single channel of lattice sites. For simplicity, we focus only on one case of solid–fluid interaction parameters, C_3. The systems considered in Fig. 6 differ in the arrangement of solid lattice sites, shown in red, around the channel. In particular, in Type I and III, each lattice site available for adsorption is surrounded either by 1 or 2 solid lattice sites. This in general creates a uniform energy profile across the channel. Effectively, the difference between these two systems is the resulting strength of solid–fluid interaction at each available site which is doubled in system III compared to I. A very different structure is associated with system II, where only every second site available for adsorption is in contact with 2 solid lattice sites. This leads to periodic (with the period of 1 lattice site) variation of the energy of solid–fluid interaction from $-2\epsilon_{sf}$ to 0. In the panel below the visualization of the structure of the system, we show the hopping rate from site to site under the steady state condition. It is clear that the systems behave very

differently. In the systems with significant energy barriers, the sites feature non-uniform density and hopping rate between the sites, unlike in systems I and III where their properties are uniform across the channel. In turn, this has significant repercussions on the behavior of the system in $\alpha_{A/B}$ vs k_A and $\alpha_{A/B}$ vs $\frac{S_A}{S_B}$ coordinates. Indeed, in systems with uniform distribution of solid sites along the channel, $\alpha_{A/B}$ is increased with k_A, as a result of stronger solid–fluid interactions on each site. This increase in $\alpha_{A/B}$ is also associated with the increase in $\frac{S_A}{S_B}$. Type II is a system with energy barriers that dramatically deviates from these trends: it features very low flux, and the perm-selectivity is effectively unity as the system does not process any separation capabilities regardless of the sorption selectivity.

What is important to understand is that in disordered polymer structure the overall behavior reflects a complex combination of I, II, III patterns discussed above and this is one of the reasons why sorption driven separations in glassy polymers do not easily conform to a single theoretical formalism.

In the second simplified example, we focus specifically on the topological effects which may lead to substantial differences in perm-selectivity and sorption selectivity behavior. For this, we consider a channel with a dead-end side-branch pore as shown in Fig. 7. In static sorption calculations, the porous space in the dead-end branch shows very high selectivity due to the strong confinement and enhanced solid–fluid interactions. However, in the non-equilibrium transport studies, we observe that under the steady state conditions, there is no flux in this branch pore and it has effectively no influence on the transport properties of this structural element as these properties are dominated by the main channel through
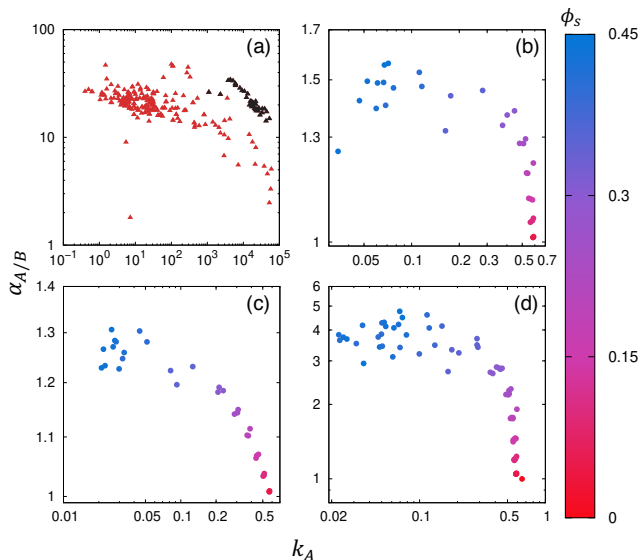
FIG. 8. Perm-selectivity ($\alpha_{A/B}$) as a function of permeability of component A (k_A). Panel (a) shows the CO_2/N_2 results from the literature and the values for PIMs are highlighted in black, where (b)–(d) corresponds to results from systems C_1–C_3, respectively. The color bar shows the solid fraction of the polymer matrix, ϕ_s.

which the fluid must pass. As a result, the effective perm-selectivity of this element can be significantly lower than the sorption selectivity, in the case of C_3, the difference is an order of magnitude between perm- and sorp- selectivity. We found that this observation depends only on the geometry and holds for all the cases of solid–fluid interaction tested. The disordered lattice structure considered previously of course does not feature such simple elements, but it contains complex regions of various sizes that exhibit high adsorption selectivity but do not influence fluid transport and resulting perm-selectivity.

With this picture in mind, let us now return to the disordered lattice matrix systems, explore their behavior in Robeson coordinates, and relate this behavior to the experimental observations.

The perm-selectivity is plotted with respect to permeability on a log–log scale in Fig. 8. Fig. 8a reports again the experimental results obtained from the literature with the PIM based membranes highlighted in black, [12–31] and panel (b)–(d) demonstrates the results for C_1–C_3, respectively. In order to emphasize the trend, percolated matrices with higher fractions of solid lattice sites have also been incorporated into the analysis.

Concentrating on the predictions from the theory, all systems considered here exhibit a similar trend where the performance cloud can be essentially divided into two regions. The first region, on the left side of each graph, is associated with low porosity structures. In this region, the systems exhibit a significant degree of scattering. However, by moving to the matrices with

higher porosities, the permeability of the structure in this regime can be increased without significant sacrifice of perm-selectivity. This process continues up to a region in permeability (or density of the structure) beyond which there is a sharp decrease in perm-selectivity. This sharp decrease constitutes the second region.

Interestingly, while the experimental data in panel (a) is a collection of results over a large number of polymers of different structures and chemical compositions, it also shows similar patterns and two regions identified by the theoretical model. Furthermore, the series of points at the transition region indicating the highest permeability while maintaining good perm-selectivity correspond to the high porosity PIM materials highlighted in black triangles.

Let us summarize the implications of our findings. Firstly, within our model, the ideal perm-selectivity obtained from permeability of individual components agrees well with the actual perm-selectivity. Using ideal perm-selectivity as a performance metric for polymer materials is a common practice in the membrane separations community. However, not all systems follow this assumption. [72] Given the very general nature of the model, we can hypothesize that to observe non-ideal effects one must include other elements into the model such as the kinetic effects.

Currently, there is no theoretical justification for the Robeson bound for sorption driven processes such as CO_2/N_2 separation. Using DMFT, we demonstrate that for what is commonly thought as an equilibrium sorption-driven separation, diffusion still plays a significant role in the separation mechanism. Using very simple models of structural elements to isolate various scenarios, we are arriving at the following conclusions, some of them deliberately more speculative than the others to prompt further theoretical and computation studies:

1. The behavior of the complex disordered structure is governed by both equilibrium and diffusion factors, with the diffusion properties being a strong function of the potential energy surface.

2. The overall transport behavior of the disordered structures is governed by the combined contributions of various structural elements and with a strong dependence on topology of the porous space. It is possible that depending on the value of permeability, a different mechanism dominates. This is why it is challenging to develop a Robeson bound for these systems within a framework of a single transport theory.

3. As a result, within the presented model, sorption selectivity is the limiting behavior that is never actually attained in the dynamic process. The perm-selectivity values are always significantly lower than sorption selectivity. This could suggest the following: if the perm-selectivity exceeds the equilibrium sorption selectivity, it indicates that the kinetic separation mechanisms are also contributing to the overall separation process.

4. The transition point between the two regimes of perm-selectivity identified in this work corresponds to

the best separation performance that can be achieved for a group of polymers with similar strength of solid–fluid interactions (in other words for polymers with similar chemistry). Interestingly, generalized for many different experimental polymer systems, this point corresponds to the PIM materials.

5. Based on the previous statement, it seems that the rational strategy to improve the performance of a group of polymers with similar solid–fluid interactions should be focused on improving their permeability characteristics. This could in principle be achieved with the addition of structuring elements (e.g. nanotubes, nanoflakes) that streamline diffusion pathways in the disordered polymers.

IV. SUPPLEMENTARY MATERIAL

The supplementary material provides additional details on the equilibrium adsorption isotherms for the polymer systems.

V. ACKNOWLEDGEMENTS

VI. AUTHOR CONTRIBUTIONS

T.Y. carried out the calculation and wrote the manuscript, T.Y., M.G.D.A., and L.S. analyzed the data and revised the manuscript.

VII. COMPETING INTERESTS

The authors declare no competing interests.

[1] M. Galizia, W. S. Chi, Z. P. Smith, T. C. Merkel, R. W. Baker, and B. D. Freeman, Macromolecules **50**, 7809 (2017).

[2] M. E. Boot-Handford, J. C. Abanades, E. J. Anthony, M. J. Blunt, S. Brandani, N. Mac Dowell, J. R. Fernández, M.-C. Ferrari, R. Gross, J. P. Hallett, *et al.*, Energy Environ. Sci **7**, 130 (2014).

[3] G. Liu, W. Jin, and N. Xu, Chem. Soc. Rev. **44**, 5016 (2015).

[4] R. K. Joshi, S. Alwarappan, M. Yoshimura, V. Sahajwalla, and Y. Nishina, Appl. Mater. Today **1**, 1 (2015).

[5] S. Qiu, M. Xue, and G. Zhu, Chem. Soc. Rev. **43**, 6116 (2014).

[6] R. S. K. Valappil, N. Ghasem, and M. Al-Marzouqi, J. Ind. Eng. Chem. **98**, 103 (2021).

[7] Z. Wu, in *Membrane Separation Principles and Applications*, Handbooks in Separation Science, edited by A. F. Ismail, M. A. Rahman, M. H. D. Othman, and T. Matsuura (Elsevier, 2019) pp. 147–179.

[8] L. M. Robeson, J. Membr. Sci. **62**, 165 (1991).

[9] L. M. Robeson, J. Membr. Sci. **320**, 390 (2008).

[10] Y. Cheng, Y. Ying, S. Japip, S.-D. Jiang, T.-S. Chung, S. Zhang, and D. Zhao, Adv. Mater. **30**, 1802401 (2018).

[11] M. Aroon, A. Ismail, T. Matsuura, and M. Montazer-Rahmati, Sep. Purif. Technol. **75**, 229 (2010).

[12] J. Park and D. Paul, J. Membr. Sci. **125**, 23 (1997).

[13] Y. Dai, M. D. Guiver, G. P. Robertson, Y. S. Kang, and K. J. Lee, Macromolecules **36**, 6807 (2003).

[14] P. M. Budd, K. J. Msayib, C. E. Tattershall, B. S. Ghanem, K. J. Reynolds, N. B. McKeown, and D. Fritsch, J. Membr. Sci. **251**, 263 (2005).

[15] Y. Shida, T. Sakaguchi, M. Shiotsuki, F. Sanda, B. D. Freeman, and T. Masuda, Macromolecules **38**, 4096 (2005).

[16] Y. Hu, T. Sakaguchi, M. Shiotsuki, F. Sanda, and T. Masuda, J. Membr. Sci. **282**, 423 (2006).

[17] Y. Shida, T. Sakaguchi, M. Shiotsuki, F. Sanda, B. D. Freeman, and T. Masuda, Macromolecules **39**, 569 (2006).

[18] F. Z. Khan, T. Sakaguchi, M. Shiotsuki, Y. Nishio, and T. Masuda, Macromolecules **39**, 6025 (2006).

[19] M. L. Cecopieri-Gómez, J. Palacios-Alquisira, and J. Dominguez, J. Membr. Sci. **293**, 53 (2007).

[20] M. M. Dal-Cin, A. Kumar, and L. Layton, J. Membr. Sci. **323**, 299 (2008).

[21] B. Comesaña-Gándara, J. Chen, C. G. Bezzu, M. Carta, I. Rose, M.-C. Ferrari, E. Esposito, A. Fuoco, J. C. Jansen, and N. B. McKeown, Energy Environ. Sci. **12**, 2733 (2019).

[22] D. Hofmann, M. Heuchel, Y. Yampolskii, V. Khotimskii, and V. Shantarovich, Macromolecules **35**, 2129 (2002).

[23] M. Heuchel, D. Hofmann, and P. Pullumbi, Macromolecules **37**, 201 (2004).

[24] X. Hu, J. Tang, A. Blasig, Y. Shen, and M. Radosz, J. Membr. Sci. **281**, 130 (2006).

[25] W. Fang, L. Zhang, and J. Jiang, J. Phys. Chem. C **115**, 14123 (2011).

[26] K.-S. Chang, K.-L. Tung, Y.-F. Lin, and H.-Y. Lin, RSC Adv. **3**, 10403 (2013).

[27] J. Zhou, X. Zhu, J. Hu, H. Liu, Y. Hu, and J. Jiang, Phys. Chem. Chem. Phys. **16**, 6075 (2014).

[28] K. Golzar, S. Amjad-Iranagh, M. Amani, and H. Modarress, J. Membr. Sci. **451**, 117 (2014).

[29] C. H. Park, E. Tocci, S. Kim, A. Kumar, Y. M. Lee, and E. Drioli, J. Phys. Chem.B **118**, 2746 (2014).

[30] H. Rabiee, A. Ghadimi, S. Abbasi, and M. T., Chem. Eng. Res. Des. **98**, 96 (2015).

[31] Y. Han and W. W. Ho, J. Membr. Sci. **628**, 119244 (2021).

[32] B. D. Freeman, Macromolecules **32**, 375 (1999).

[33] A. Y. Alentiev and Y. P. Yampolskii, J. Membr. Sci. **165**, 201 (2000).

[34] L. Robeson, B. Freeman, D. Paul, and B. Rowe, J. Membr. Sci. **341**, 178 (2009).

[35] B. W. Rowe, L. M. Robeson, B. D. Freeman, and D. R. Paul, J. Membr. Sci. **360**, 58 (2010).

[36] A. Alentiev and Y. Yampolskii, Ind. Eng. Chem. Res. **52**, 8864 (2013).

[37] M. De Angelis, G. Sarti, and F. Doghieri, J. Membr. Sci. **289**, 106 (2007).

[38] M. G. De Angelis, G. C. Sarti, and F. Doghieri, Ind. Eng. Chem. Res. **46**, 7645 (2007).

[39] B. Smit, J. A. Reimer, C. M. Oldenburg, and I. C. Bourg, *Introduction to carbon capture and sequestration*, Vol. 1 (World Scientific, 2014).

[40] N. Vergadou and D. N. Theodorou, Membranes **9**, 98 (2019).

[41] G. Yilmaz and S. Keskin, Ind. Eng. Chem. Res. **51**, 14218 (2012).

[42] A. Ozcan, C. Perego, M. Salvalaglio, M. Parrinello, and O. Yazaydin, Chem. Sci. **8**, 3858 (2017).

[43] A. Ozcan, R. Semino, G. Maurin, and A. O. Yazaydin, Chem. Mater. **32**, 1288 (2020).

[44] B. Comesaña-Gandara, L. Ansaloni, Y. Lee, A. Lozano, and M. De Angelis, J. Membr. Sci. **542**, 439 (2017).

[45] H. Wu, J. Thibault, and B. Kruczek, J. Membr. Sci. **618**, 118715 (2021).

[46] S. Mohsenpour, Z. Guo, F. Almansour, S. M. Holmes, P. M. Budd, and P. Gorgojo, J. Membr. Sci. **661**, 120889 (2022).

[47] P. A. Monson, J. Chem. Phys. **128**, 084701 (2008).

[48] J. R. Edison and P. A. Monson, Langmuir **29**, 13808 (2013).

[49] G. L. Aranovich and M. D. Donohue, Phys. Rev. E **60**, 5552 (1999).

[50] L. Sarkisov and P. A. Monson, Phys. Rev. E **65**, 011202 (2001).

[51] H.-J. Woo, L. Sarkisov, and P. A. Monson, Langmuir **17**, 7472 (2001).

[52] E. Kierlik, P. A. Monson, M. L. Rosinberg, L. Sarkisov, and G. Tarjus, Phys. Rev. Lett. **87**, 055701 (2001).

[53] H.-J. Woo, L. Sarkisov, and P. Monson, in *Characterization of Porous Solids VI*, Studies in Surface Science and Catalysis, Vol. 144 (Elsevier, 2002) pp. 155–162.

[54] C. Sangwichien, G. L. Aranovich, and M. D. Donohue, Colloids Surf. A Physicochem. Eng. Asp. **206**, 313 (2002).

[55] D. Matuszak, G. L. Aranovich, and M. D. Donohue, J. Chem. Phys. **121**, 426 (2004).

[56] D. Matuszak, G. L. Aranovich, and M. D. Donohue, J. Non-Equilib. Thermodyn. **31** (2006).

[57] D. Matuszak, G. L. Aranovich, and M. D. Donohue, Phys. Chem. Chem. Phys. **8**, 1663 (2006).

[58] P. A. Monson, Langmuir **24**, 12295 (2008).

[59] J. R. Edison and P. A. Monson, J. Low Temp. Phys. **157**, 395 (2009).

[60] J. R. Edison and P. A. Monson, Faraday Discuss. **146**, 167 (2010).

[61] J. R. Whitman, G. L. Aranovich, and M. D. Donohue, J. Chem. Phys. **134**, 094303 (2011).

[62] J. R. Edison and P. A. Monson, Microporous Mesoporous Mater. **154**, 7 (2012).

[63] J. R. Edison and P. A. Monson, J. Chem. Phys. **138**, 234709 (2013).

[64] A. Rathi, J. R. Edison, D. M. Ford, and P. A. Monson, AIChE J **61**, 2958 (2015).

[65] A. Rathi, E. Kikkinides, D. Ford, and P. A. Monson, Langmuir **35**, 5702 (2019).

[66] A. Desouza and P. A. Monson, Adsorption **27**, 253 (2021).

[67] D. N. Lapshin, A. V. Gromov, E. E. Campbell, and L. Sarkisov, J. Phys. Chem. C **125**, 21254 (2021).

[68] E. Kikkinides, G. Gkogkos, P. Monson, and R. Valiullin, J. Chem. Phys. **156**, 134702 (2022).

[69] T. Yuan, A. H. Farmahini, and L. Sarkisov, J. Chem. Phys. **155**, 074702 (2021).

[70] T. Yuan and L. Sarkisov, Adv. Theory Simul. **5**, 2200159 (2022).

[71] J.-F. Gouyet, M. Plapp, W. Dieterich, and P. Maass, Adv. Phys. **52**, 523 (2003).

[72] E. Ricci, M. Minelli, and M. G. De Angelis, Membranes **12**, 857 (2022).

[73] C. R. Mason, L. Maynard-Atem, K. W. Heard, B. Satilmis, P. M. Budd, K. Friess, M. Lanč, P. Bernardo, G. Clarizia, and J. C. Jansen, Macromolecules **47**, 1021 (2014).